Highly Efficient Near-Field to Far-Field Transform for Polar Near-Field Scanned Data

S.F. Gregson[1, 2]
[1]Next Phase Measurements
11521 Monarch St, Garden Grove, CA, USA
stuart.gregson@npmeas.com

C.G. Parini[2]
[2]Electronic Engineering & Computer Science
Queen Mary University of London
London, UK
c.g.parini@qmul.ac.uk

B. Pyne[3], H. Saito[3], K. Tanaka[3]
[3]Department of Spacecraft Engineering,
Institute of Space and Astronautical Science (ISAS),
Japan Aerospace Exploration Agency (JAXA)
bupyn@synspective.com
saito.hirobumi@aoni.waseda.jp
tanaka.koji@jaxa.jp

***Abstract*—Despite being a comparatively uncommonly encountered near-field antenna measurement configuration, plane-polar systems are important as they present certain distinctive and very attractive attributes. These include mechanical simplicity and the ability to acquire near-field data across acquisition intervals that are potentially far larger than the measurement system itself or the test chamber in which it is situated. They do however require specialist near-field to far-field data transformation algorithms which can pose implementation challenges in terms of numerical accuracy and computational efficiency. This paper presents a new, efficient, rigorous, data transformation algorithm that can also transform data acquired over rotationally symmetric, non-planar measurement surfaces. The new, accelerated, Fourier-Bessel based transform is verified through numerical simulation and its successful application in transforming measured data of a high gain, passive, space-borne synthetic aperture radar (SAR) antenna is highlighted.**

I. Introduction

The plane-polar approach for near-field antenna measurements has attracted a great deal of interest in the open literature during the past four decades [1, 2, 3, 4, 5, 6, 7] since its first inception. The measurement system is formed from the intersection of a linear translation stage and a rotation stage with the combination of the axes enabling the scanning near-field probe to trace out a radial vector in two-dimensions facilitating the acquisition of samples across the surface of a planar disk, typically being tabulated on a set of concentric rings, as shown in Figure 1. In its classical form, the probe moves in a fixed radial direction and the AUT rotates axially. However, with the ever more prevalent utilization of industrial multi-axis robots or uninhabited air vehicles (UAV), *i.e.* drones, being harnessed for the task of mechanical probe positioning; non-planar, polar measurements are feasible and are becoming more common. An example test system comprising two industrial multi-axis robots can be seen illustrated in Figure 1. Here, robot 1, R_1, is used for plane-polar radius (or diameter) scanning of the probe along a *circa* 6 m long radius, which provides a 12 m diameter plane polar acquisition disk scan size. Robot 2, R_2, holds the AUT and is used to provide the 360° ϕ-axis rotation. A clear advantage of this measurement concept, and the accompanying transform presented below, is that it enables acquisitions to be taken easily over rotationally symmetrical, conformal surfaces, *i.e.* admitting the ability of utilizing non-planar polar geometries thereby minimizing truncation errors and maximizing the ability of the system to predict wide-out side-lobe patterns without needing to increase the measurement size.

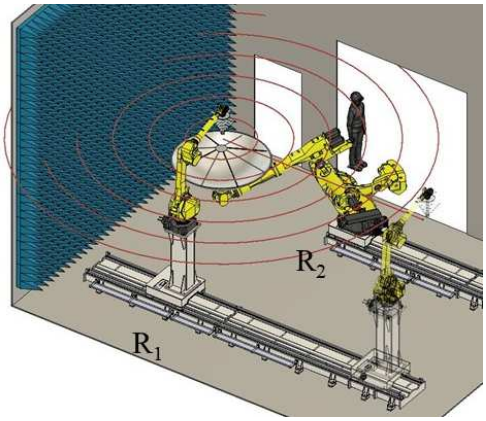

Figure 1. Illustration of plane-polar antenna measurement using dual multi-axis industrial robots

The successful deployment of this concept is clearly predicated upon the availability of a suitable data transformation algorithm. In this paper, an accelerated, rigorous, near-field to far-field transform that is based on a Fourier-Bessel expansion [4] is developed and presented that can be employed in the above circumstances. This highly efficient, robust, transform enables near-field data acquired on planar, and non-planar, surfaces to be transformed to the far-field providing the acquisition surface is rotationally symmetric about some fixed point in the x,y-plane with the z distance being purely a function of the radial displacement. The transform efficiency stems from the utilization of the fast Fourier transform (FFT) algorithm with the rigor and robustness deriving from the avoidance of recourse to approximation, *e.g.* piecewise polynomial interpolation. Specifically, this algorithm does not rely upon approximation, *i.e.* interpolation, to re-grid the plane-polar measured data prior

to FFT processing. This transform is numerically equivalent to a discrete Fourier transform, but is approximately 1000 times faster, and can rigorously transform near-field data of electrically large antennas to the far-field in a few seconds. Section 2 presents an overview of the transformation algorithm with results of the validation campaign and actual range measurements being presented in Section 3. The paper concludes with Section 4 which includes a summary of the results, and the transform's assumptions and requirements.

II. Overview of the Fourier Bessel Polar Near-Field to Far-Field Transform

As the transformation from Cartesian to plane-polar co-ordinates is a one-to-one mapping, the analytic functions are continuous, the necessary partial derivatives exist and are continuous, and assuming the initial boundary conditions are specified so that $\rho' \geq 0$ (this is not a practical limitation) with $x = \rho'\cos\phi'$, $y = \rho'\sin\phi'$, with z = arbitrary but fixed, then through a multi-dimensional exchange of variables, we can for each tangential component relate the angular spectrum to the near electric field through [8],

$$F(\theta,\phi) = \int_0^{2\pi}\int_0^{\infty} f(\rho',\phi') e^{jk_0\rho'\sin\theta\cos(\phi'-\phi)} \rho' d\rho' d\phi' \tag{1}$$

where we have used primed variables to denote the near-field coordinates. This expression can be evaluated numerically as, through an application of the sampling theorem, it can be represented as a summation for the case where band-limited antennas are considered [6]. With this noted, it is desirable to present this in an alternative form allowing us to harness the far more efficient FFT algorithm.

Following reference [4], and for the sake of simplicity, let us first assume that the probe is omnidirectional so that we may omit probe compensation. Note, this restriction is introduced for the sake of pedagogy and will be relaxed shortly to obtain the general, accelerated, probe-compensated plane-polar near-field to far-field transformation. Let us now consider expressing the integral in the form of a correlation process [9] which can be considered to form the basis of any antenna pattern measurement. This stems from recognizing that the correlation of the measured field of some antenna to a plane-wave propagating in an arbitrary, but known, direction, say (θ, ϕ), *is* the far-field pattern of that antenna, in that direction. To further simply the development, let us also consider the contribution to the far-field pattern of just a *single* ring of near-field data taken at measurement radius ρ'. Thus, the far-field contribution of this n^{th} ring at radius ρ' is,

$$F_n(\theta,\phi=\phi') = f(\rho_n',\phi=\phi')\rho_n' \otimes L_n(\theta,\phi=\phi') \tag{2}$$

Here $\otimes$ denotes the correlation operation [9] and where, in the one-dimensional azimuthal case considered here, the coupling plane-wave can be expressed as,

$$L_n(\theta,\phi') = e^{jk_0\rho_n'\sin\theta\cos\phi'} \tag{3}$$

The one-dimensional FFT can be used to implement the cross-correlation operation numerically by using the Wiener-Khintchine theorem [9], where if the Fourier transform of $R(\tau)$ is $F(\omega)$ then,

$$\Im\{R_1(\tau)\otimes R_2(\tau)\} = F_1(\omega)\cdot F_2(-\omega) \tag{4}$$

Thus, we may write that,

$$F_n(\theta,\phi=\phi') = \Im^{-1}\{\Im\{f(\rho_n',\phi')\rho_n'\} \cdot \Im\{L_n(\theta,\phi')\}\} \tag{5}$$

Here, $\Im$ denotes the Fourier transform operation and $\Im^{-1}$ denotes the inverse operation. Note, as we take the cosine of the variable ϕ', and as the cosine function is an even function, we may omit the minus sign on the variable ϕ'. The linearity of the inverse Fourier transform operation enables us to obtain the complete far-field pattern by summation across each of the N rings of near-field plane-polar data prior to taking the inverse Fourier transform. Thus, we may write the total far-field pattern as the linear superposition,

$$F(\theta,\phi=\phi') = \Im^{-1}\left\{\sum_{n=1}^{N}\Im\{f(\rho_n',\phi')\rho_n'\} \cdot \Im\{L_n(\theta,\phi')\}\right\} \tag{6}$$

Here N is the number of near-field rings of plane-polar data and the "dot" symbol, $\cdot$, merely denotes scalar multiplication. Thus, the plane-polar near-field to far-field transform can be expressed compactly as,

$$F(\theta,\phi=\phi',z=d) = e^{jk_0 d\cos\theta} \Im^{-1}\left\{\sum_{n=1}^{N}\Im\{f(\rho_n',\phi')\rho_n'\} \cdot \Im\{e^{jk_0\rho_n'\sin\theta\cos\phi'}\}\rho_n'\delta\rho'\delta\phi'\right\} \tag{7}$$

Here, d denotes the separation distance between the AUT aperture and the plane-polar acquisition disk located at the tip of the near-field probe, $\delta\rho'$ denotes the sample spacing in the radial axis, and $\delta\phi'$ denotes the sample spacing in the angular, *i.e.* azimuthal axis. The Fourier transforms and the inverse Fourier transform can be evaluated efficiently using the one-dimensional FFT. In the event the number of angular samples is not an integer power of two, then a mixed-radix version of the FFT and inverse fast Fourier transform (IFFT) algorithms must be utilized. As has been noted before [8], the $\rho' = 0$ cut, *i.e.* which is when $n = 1$, is a special case where the elemental area of the "cap" should be used to weight the correlated cut prior to it being summed. Thus, we may obtain the plane-wave spectrum from plane-polar near-field data using an efficient FFT based algorithm. Two points are important to recognize here. Firstly, the series of one-dimensional mixed-radix transforms of the near-electric-field components can be pre-computed and stored prior to entering the radial summation. Secondly, the Fourier transform of the L_n can be computed analytically which greatly increases the accuracy and speed of this transform as there is no need to perform a, comparatively, computationally intensive one-dimensional mixed-radix FFT $N\times n_\theta$ times. Additionally, the series of inverse one-dimensional Fourier transforms can be sped-up significantly by zero-padding the Fourier coefficient data to make the number of points comprise an integer power of two, whereupon the far more efficient power-of-two inverse fast Fourier transform can be brought to bear.

To establish the analytical transformation of the L_n function, and so as to simplify the notation, let us write the complex exponential in terms of new variables as,

$$e^{jk_0\rho'_n \sin\theta\cos\phi'} = e^{j\alpha\cos\phi'} \tag{8}$$

This can be expanded in terms of a series of Bessel functions as,

$$\begin{aligned} e^{j\alpha\cos\phi'} &= J_0(\alpha) \\ &\quad -2\left(J_2(\alpha)\cos(2\phi') - J_4(\alpha)\cos(4\phi')\right. \\ &\quad \left. +J_6(\alpha)\cos(6\phi') + \cdots\right) \\ &\quad +2j\left(J_1(\alpha)\cos(\phi') - J_3(\alpha)\cos(3\phi')\right. \\ &\quad \left. +J_5(\alpha)\cos(5\phi') + \cdots\right) \end{aligned} \tag{9}$$

A comparison of this series and the analytical function can be seen presented in the following figure where just the first 15 terms have been used in the Bessel function series.

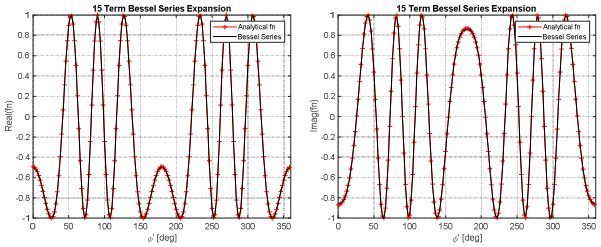

Figure 2. Comparison of series solution and complex exponential function. Left: real part; Right: imaginary part.

The Fourier transform of this series can then be obtained by noting that the Bessel functions are a constant with respect to the Fourier variable, ϕ′, thus the first term of the series corresponds to a Dirac delta function scaled by the amplitude of the zeroth order Bessel function $J_0(\alpha)$, and located at the Nyquist frequency, and secondly that the Fourier transform of a cosine function comprises a pair of Dirac delta functions positioned at complimentary frequencies about the Nyquist frequency. Thus, the remaining terms in the series each transform to a pair of discrete integer frequencies with amplitude scaled by the associated Bessel function, *i.e.*,

$$\begin{aligned} \Im\left\{e^{j\alpha\cos\phi'}\right\} = n_\phi\big[&J_0(\alpha), jJ_1(\alpha), j^2J_2(\alpha), \ldots, \\ &j^2J_2(\alpha), jJ_1(\alpha)\big] \end{aligned} \tag{10}$$

This enables the rapid, accurate, computation of this transform and can be seen illustrated with the black trace in Figure 3 where there were 60 points in each ring of near-field data, 30 terms were used in the series, and a mixed-radix one-dimensional FFT was used to transform the complex exponential function which is denoted by the red trace and included as a comparison.

It is important to recognize that in practice; Bessel functions such as these are computed using recurrence relations requiring only the first couple of terms in the series to be directly computed, with all other terms being obtained from these values with renormalization utilized to retain numerical precision when high order coefficients are required.

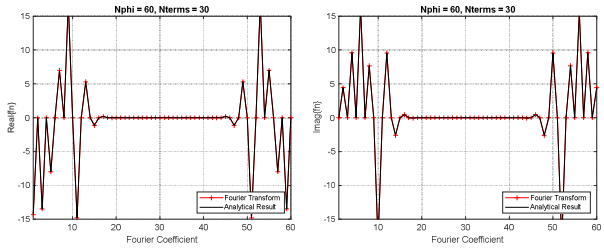

Figure 3. Comparison of Fourier transformed complex exponential function and analytical solution, Left: real part; Right: imaginary part.

A further, very powerful, consequence of this formulation is that it is automatically in a form for processing data that is acquired on non-planar surfaces providing only that the smooth acquisition surface is rotationally symmetrical about the positive *z*-axis, *i.e.* providing it is of the form,

$$z'_n(\rho'_n, \phi') = z'_n\left(\sqrt{x'^2_n + y'^2_n}\right) \tag{11}$$

Here z'_n is a smooth, single valued, function of the radius coordinate ρ'_n only. Thus, the spectrum can be expressed as,

$$\begin{aligned} F(\theta, \phi = \phi', z = d) = \Im^{-1}\Bigg\{&\sum_{n=1}^{N} \Im\left\{f(\rho'_n, \phi')\rho'_n\right\} \\ &\cdot \Im\left\{e^{jk_0(\rho'_n \sin\theta\cos\phi' + z'_n\cos\theta)}\right\} \\ &\cdot \rho'_n \delta\rho' \delta\phi'\Bigg\} \end{aligned} \tag{12}$$

Where the corresponding far-electric-fields can be obtained from [8],

$$\underline{E}(\theta, \phi) \approx \frac{j\cos\theta}{2\pi} \underline{F}(\theta, \phi) \frac{e^{-jk_0 r}}{r} \tag{13}$$

This is of particular utility to drone testing where acquisitions are routinely taken in a series of concentric rings around AUT where each ring is at a different altitude. Additionally, the zero-padding processing utilized within this accelerated transform means that each ring may be acquired with a *different* number of points which is important as the number of acquired data-points has a bearing on the flight-time of the drone which is crucially dependent upon, and limited by, battery life. The longitudinal field component can be obtained from the plane-wave condition and the magnetic field can then be obtained from the electric field and the impedance of free-space. The fields may be resolved onto whichever polarization basis desired, *e.g.* Ludwig's 3rd definition [8], *etc.* and can be converted to left- and right-hand circular polarization components, tilt angle, polarization ratios if required. As noted at the beginning of this development, the probe corrected far-electric-field data may be obtained from these spectra using standard planar probe pattern compensation providing a rotationally symmetrical, *i.e.* first order, probe is used; or alternatively, if a more general near-field probe is utilized but counter rotated during the acquisition process so as to remain polarization matched to the AUT during the acquisition when taking each orthogonal tangential near-field component [8].

The next section presents results of the validation of this transform before progressing to examine results from actual range measurements.

III. RESULTS

The use of this Fourier Bessel transform can be illustrated by taking simulated plane-polar near-field data and transforming it to the far-field whereupon it can be compared with fields that we computed using a standard discrete Fourier transform (DFT) [8] and those far-fields obtained directly from the simulation software. Figure 4 present simulated plane-polar near-electric-field components of a parabolic reflector antenna radiating at C-band for the two orthogonal tangential polarizations E_x (left) and E_y (right). Here, the horizontal axis is the measurement radius ρ' and the vertical axis is the polar angle ϕ' in degrees.

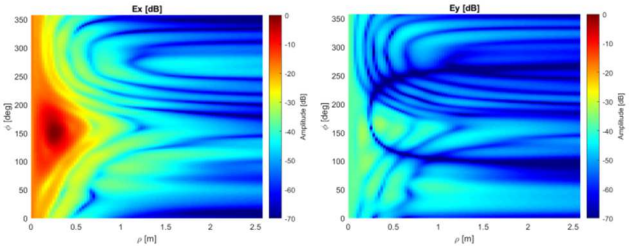

Figure 4. *x*- and *y*-polarised near-electric fields of a offset-reflector antenna tabulated on a plane-polar grid.

The algorithm developed in Section 2 was used to transform the near-electric-field data to the far-field with the resulting data being compared to data provided by a DFT and ideal data provided directly in the far-field from reflector antenna simulation software. An off-pointed parabolic reflector antenna was used as the AUT where the rotation of the antenna with respect to the acquisition plane was deliberate and intended to make sure that any symmetry within the simulated measurement would be broken.

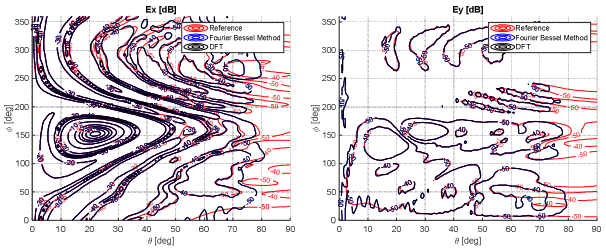

Figure 5. Comparison iso-level plot of co-polar and cross-polar far-electric-fields.

Figure 5 presents far-field iso-level plots provided by an antenna simulation (red contours) the far-fields provided by a conventional discrete Fourier transform (black contours) and far-fields provided by the accelerated Fourier Bessel transform (blue contours). From inspection of Figure 5 it can be seen that the contours of the accelerated Fourier Bessel transform pattern agree very well with those of the discrete Fourier transform, *i.e.* there are no observable differences. These patterns also agree well with the far-fields obtained directly from the simulation software with differences resulting from the first and second order truncation effects which generally become more pronounced at wider pattern angles. As a further test, the polar acquisition surface was deformed into a curved "cap". The *x*-polarized near-electric-field component can be seen presented in the form of a false-color surface plot in Figure 6.

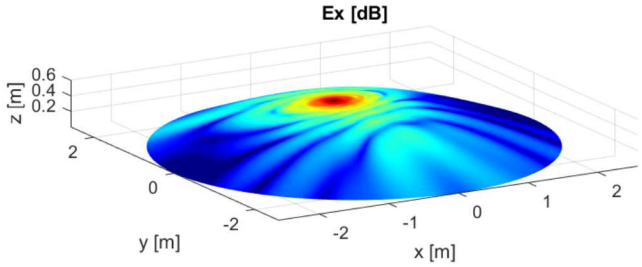

Figure 6. *x*-polarised near electric field of offset reflector antenna sampled across a circular cap.

This data was transformed to the far-field and compared again with far-field data obtained from the DFT and the direct far-fields.

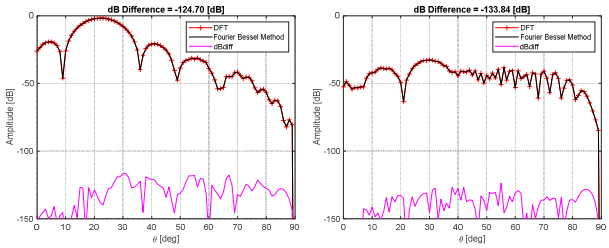

Figure 7. Comparison of far-field amplitude pattern from accelerated Fourier Bessel transform and DFT

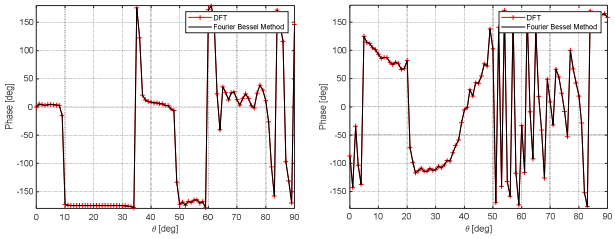

Figure 8. Comparison of far-field phase pattern from accelerated Fourier Bessel transform and DFT

Figure 7 presents a comparison of the co-polar (left) and cross-polar (right) cardinal cuts together with the dB difference level. Here, it can be seen that again, the patterns are in excellent agreement with the root mean square (RMS) dB difference level over the entire far-hemisphere better than -120 dB, which is *circa* 50 dB below the next smallest component within a typical range uncertainty budget. Here, the accelerated transform took ~0.5 seconds to run, which was approximately 0.1% (*i.e.* one thousandth) of the time that the DFT took to calculate the equivalent far-field data running on the same workstation. Figure 8 presents a similar plot comparison of the far-field phase functions which from inspection are equally encouraging.

As the computational electromagnetic measurement simulations yielded such encouraging results, the new transform was harnessed to process plane-polar near-field measurements of an *x*-band 4.9 m wide, seven tile, passive, planar, space-born, slotted array, synthetic aperture radar (SAR) antenna which is shown undergoing assembly integration and test in Figure 9 with details of the antenna and mission being available in the open literature, *e.g.* [10, 11].

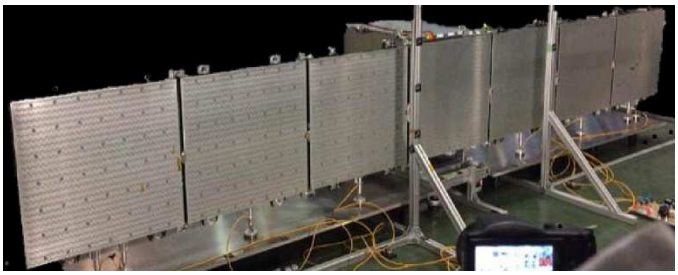

Figure 9. StriX α deployed 4.9 m x 0.7 m, X-band, 7 panel, synthetic aperture radar, undergoing deplyment test.

The measured near-field amplitude (left) and phase (right) of the antenna at 9.65 GHz can be found presented in Figure 10, where the horizontal axis represents the measurement radius, and the vertical axis the polar angle in degrees. This antenna comprises a demanding measurement as the antenna's electrical size corresponds to a high-gain (~44.5dBi) "sharp" far-field antenna pattern requiring correct sampling, and a reliable modal expansion, *cf.* Section 2 above.

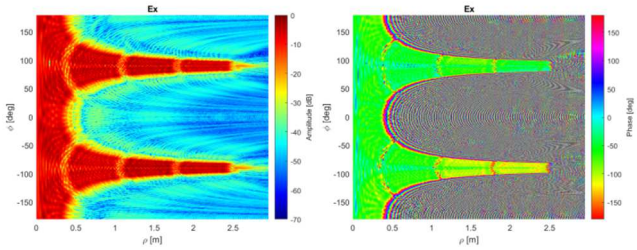

Figure 10. plane-polar amplitude (left) and phase(right) of a 5m wide X-band passive SAR antenna

The classical plane-polar, half wavelength circumference sampling criteria in the angular axis may be expressed as [6],

$$\Delta\phi' = \lambda/2(a+\lambda) = \pi/M \qquad (14)$$

Here, a is the maximum radial extent (MRE), *i.e.* the circumscribing radius of the antenna measured from the center of rotation which must be less than the maximum radius of the acquisition disk. In the event that the AUT exhibits rotational symmetry then this criteria may be relaxed. We can interpret M as the maximum order of Bessel function, *cf.* spherical sampling theory, which we can use to place an upper limit on the maximum number of terms required, and the number of angular measurement points. Furthermore, we are able to vary this over the radial summation as this represents an upper limit, and as we require fewer terms when processing central rings, *cf.* Figure 11. Explicitly, we may use,

$$M = \begin{cases} k_0(\rho_n + \lambda) & \text{when } \rho_n < a \\ k_0(a+\lambda) & \text{elsewhere} \end{cases} \qquad (15)$$

Where M is understood to be the nearest integer rounded towards positive infinity with the constraint that $M < (n_\phi - 2)/2$, which represents the highest order mode that may be computed from the measured data. Here, we are using a safety factor of one wavelength which corresponds to adding ~6 additional terms, *cf.* the spherical case [6], where here we have the benefit of scaling the "safety factor" with increasing frequency as opposed to being a fixed integer, *e.g.* 10. However, M should be estimated prior to commencing the near-field acquisition to insure reliable far-field data can be obtained. Figure 11 contains a plot of the magnitude of the Fourier coefficients of the plane-polar measurement (as shown in Figure 10) presented in the form of a false color plot where, it is clear that as the measurement radius increases, there is a larger amount of power contained within higher order Fourier coefficients. Here, the zero-order term has been shifted to the center of the mode spectrum. Note the symmetry observed here is a result of the behavior of the Fourier transform and specifically, the symmetry of the transform of the cosine function, *cf.* equation 10 above. The right hand side of Figure 11 shows the same spectrum only here the higher order modes have been extracted to illustrate that equation (15) reflects the natural behavior.

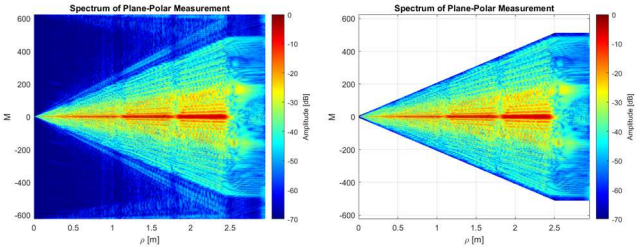

Figure 11. False colour plot of power in Fourier coefficients plotted as a function of measurement radius (left), again with higher order modes extracted as per eqn (15) (right).

The plane-polar near-field data was transformed to the far-field using the transformation developed above and can be seen presented in Figure 12. Here, the far-fields are presented tabulated on a polar spherical grid (left) and on a true-view grid (right) [8].

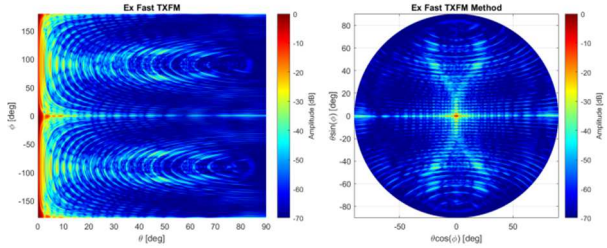

Figure 12. Far-field amplitude pattern presented in polar format (left), and in true-view format (right).

Here, the very "sharp" form of the far-field pattern, *i.e.* the very narrow beam-width and the complex side-lobe structure is clearly evident. Once the plane-wave spectrum is obtained, it is possible to compensate for the separation between the AUT and the probe, and to reconstruct the corresponding radiating aperture illumination function [8]. This can be seen presented in Figure 13 which contains the amplitude (a) and phase (b). Here, the seven individual radiating panels of the SAR antenna, *cf.* Figure 9, can be seen clearly in both the amplitude and phase pattern functions. However, it is also possible to see a small phase step in the phase of the lower two tiles which was a feature that was identified and remedied during the phase adjustment that was performed on each panel prior to launch. The use of this sort of non-invasive, non-destructive diagnostic post-processing is commonplace for the configuration of passive array antennas [8]. However its success, crucially, is predicated upon the reliable determination of the plane-wave spectrum through the use of rigorous transformation algorithms such as that which is being employed here. Conversely, Figure 13(c-d) shows the transformed far-field patterns in elevation and azimuth respectively. There is a periodic region of no-

slots at the junction between two adjacent panels which leads to periodic grating-like side-lobes appearing in the 1D far-field azimuth pattern seen in Figure 13(c). However, since these grating lobes are below -15dB, the impact on azimuth ambiguity during SAR imagery acquisition is insignificant as seen in [12]. Here it may be concluded that Fourier-Bessel pattern is more reliable since there is no approximation, *i.e.* polynomial interpolation, error.

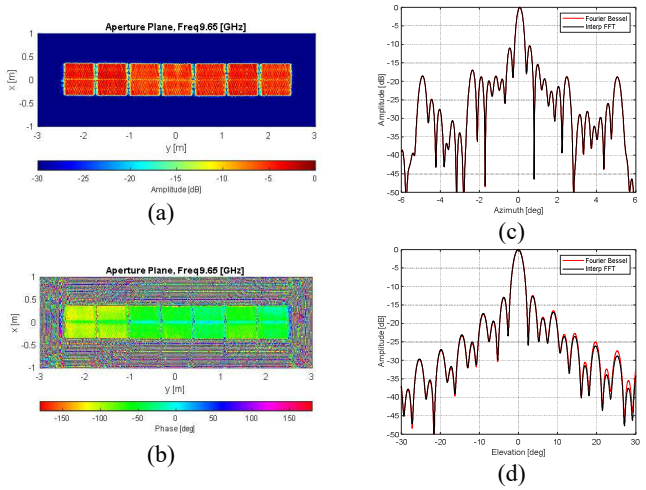

Figure 13. Reconstructed near-field (aperture plane) amplitude (a) & phase (b), transformed far-field amplitude azimuth cut (c) & elevation cut (d).

IV. Summary and Conclusion

In the previous sections a new, rigorous, computationally efficient accelerated Fourier Bessel polar near-field to far-field transform has been developed. Preliminary simulated data was used to verify and validate the planar and non-planar polar transforms against known reference data. Based upon this success, the algorithm was used to process range measurements of a high gain passive slot-array SAR antenna yielding encouraging results in this demanding application. The new transform is based on the following assumptions: either a rotationally symmetric first order probe is used [6], or the probe is counter rotated during the near-field acquisition [8], that the data is acquired using fixed $\delta\rho'$ and $\delta\phi'$ per ϕ cut (this is in common with other applications and is not a limitation of this particular implementation per se), and that a positive (suppressed) time dependency is assumed throughout. It is also worth remembering that a mixed-radix 1D FFT is used to implement the initial ϕ transform of the measured near-electric-fields. Utilizing a factor of 2 FFT and zero padding the polar near-field data will yield erroneous results. This is also the reason for the requirement that the data is periodic in the ϕ-axis, *cf.* spherical case, and does not span the full 2π radian range with redundant points at both $\phi' = 0$ and $\phi' = 2\pi$. And, lastly, that this transform is rigorous, *i.e.* it does *not* rely upon approximation, *e.g.* piecewise polynomial interpolation, least squares fitting, the solution of a linear system of simultaneous equations, *etc*. Although the far-field data will be provided tabulated on an equally spaced grid of points in the ϕ-axis (that will contain a power of 2 points) the user is free to specify the number and location of points in the θ-axis. This can be very convenient in applications such as that presented above where we are free to compute large number of points around the boresight direction of a high gain antenna without needing to compute large amounts of data at other angles that are perhaps not of interest.

It is crucial to recognize that this transform is extremely efficient with run times on the order of *circa* 0.1% of the time that it would take for an equivalent discrete Fourier transform to compute equivalent far-field data, and that are often faster than when using interpolation and two-dimensional FFT based algorithms which require large amounts of zero-padding to obtain the density of data points about the main beam direction required to reliably produce main-beam information such as beam-width, null-depth and first side-lobe level and location.

The future work is to include examining in greater detail the behavior of the Fourier coefficients, *cf.* Figure 11 above, with a view to exploring ways in which this can be used to improve the accuracy of the measurement by extracting non-physical features.

Acknowledgement

The authors gratefully acknowledge the very valuable support of Bernd Gabler of German Aerospace Center (DLR).

References

[1] Y. Rahmat SamiI, V. Galindo-Israel, R. Mittra, "A plane-polar approach for far-field reconstruction from near-field measurements", IEEE Trans., 1977, AP-25,pp. 631-641.

[2] V. Galindo-Israel, Y. Rahmat-Samii, R. Mittra, "A Plane-Polar Approach For Far-Field Reconstruction From Near-Field Measurements", Int. IEEE / AP-S Symp., Seattle, June, (1979).

[3] C.F. Stubenrauch, "Planar near-field scanning in polar coordinates: A feasibility study", NBS Rep. SR-723-73-80, 1980.

[4] J.C. Bennett, "Fast Algorithm for the Calculation of Radiation Integral and its Application to Plane-Polar Near-Field/Far-Field Transformations", Electronic Letters, 11th April 1985, Vol. 21 No. 8, pp. 343-344.

[5] P.F. Wacker, R. Severyns, "Near-field Analysis and Measurement: Plane Polar Scanning", IEE Conf. Pub. 219, Pt 1., pp.105-107 1983.

[6] A.D. Yaghjian, "An Overview of Near-Field Antenna Measurements", IEEE Trans., 1986, AP-34, pp. 3 W 5

[7] M.S. Gatti, Y. Rahmat-Samii, "FFT Applications to Plane-Polar Near-Field Antenna Measurements", IEEE Transactions on Antennas and Propagation, AP-36, June, pp. 781-791, (1988).

[8] S.F. Gregson, J. McCormick, C.G. Parini, "Principles of Planar Near-Field Antenna Measurements", IET Press, 2007, pp. 93, ISBN 978-0-86341-736-8.

[9] H.P. Hsu, "Applied Fourier Analysis", Harcourt Brace, College outline Series, ISBN 0-15-601609-5, 1984.

[10] B. Pyne, H. Saito, P. R. Akbar, K. Tanaka, J. Hirokawa and T. Tomura, "Flight Model 7-Panel Slot-Array Deployable Antenna Measurement Results of MicroX-SAR 100kg Class Demonstration Satellite," 2020 50th European Microwave Conference (EuMC), 2021, pp. 816-819, doi: 10.23919/EuMC48046.2021.9338188.

[11] B. Pyne, P. R. Akbar, V. Ravindra, H. Saito, J. Hirokawa and T. Fukami, "Slot-Array Antenna Feeder Network for Space-Borne X-Band Synthetic Aperture Radar," in IEEE Transactions on Antennas and Propagation, vol. 66, no. 7, pp. 3463-3474, July 2018, doi: 10.1109/TAP.2018.2829805.

[12] B. Pyne, H. Saito, P. R. Akbar, J. Hirokawa, T. Tomura and K. Tanaka, "Development and Performance Evaluation of Small SAR System for 100-kg Class Satellite," in IEEE Journal of Selected Topics in Applied Earth Observations and Remote Sensing, vol. 13, pp. 3879-3891, 2020, doi: 10.1109/JSTARS.2020.3006396